KSME

Springer

Journal of Mechanical Science and Technology 38 (5) 2024

Original Article
DOI 10.1007/s12206-024-0427-z

Keywords:
· Flow characteristics
· Indoor airflow
· Large-eddy simulation
· Orifice formula

Correspondence to:
Changhoon Lee
clee@yonsei.ac.kr

Citation:
Nam, J., Nam, H., Lee, C. (2024). Large-eddy simulation for indoor flow in a multizone environment. Journal of Mechanical Science and Technology 38 (5) (2024) 2485~2494.
http://doi.org/10.1007/s12206-024-0427-z

Received September 4th, 2023
Revised January 7th, 2024
Accepted January 21st, 2024

† Recommended by Editor
Han Seo Ko

Large-eddy simulation for indoor flow in a multizone environment

Jaewook Nam[1], Hyunwoo Nam[2] and Changhoon Lee[1,3]

[1]School of Mathematics and Computing, Yonsei University, Seoul 03722, Korea, [2]Agency for Defense Development, Daejeon 34186, Korea, [3]Department of Mechanical Engineering, Yonsei University, Seoul 03722, Korea

Abstract We used large-eddy simulation (LES) to numerically simulate two differently driven indoor airflows occurring in a multizone environment. In the first case, air flowed from one zone to another through a small hole driven by the total pressure difference. In the second case, unbalanced airflows arose from the buoyancy effect, which was generated by a heat source present in a specific location. To validate the LES prediction for the indoor flow analysis, we compared our simulation results with the chamber facility experimental results and other simulation results. Based on this validation, we confirmed that the LES reliably simulates indoor airflow. In addition, we discussed the flow characteristics and investigated the feasibility of modeling the flow rate through openings using an orifice formula.

1. Introduction

Accurate prediction of urban flow, both outdoors and indoors, is extremely important for predicting pollutant dispersion. Owing to the recent development of computational resources, large eddy simulation (LES) has enabled a relatively accurate prediction of outdoor flow that usually occurs in a building environment [1-7]. A real-time prediction was attempted using GPU parallelization [4]. However, relatively little effort has been devoted to simulating the indoor flows that frequently occur in multi-zone environments. As people spend most of their time indoors, the prediction of indoor flow critically determines pollutant dispersion, which is important for air quality control or evacuation in case of an accident, such as a fire or toxic gas leak.

To predict air flows in a multizone environment in a building, a network model called CONTAM was developed and is widely used [8-11]. However, because CONTAM adopts the lumped system approach under the assumption that the pressure and temperature of each zone (room) are uniform and air motion is neglected, the effect of airflow is not properly considered. Wang et al. [12] presented an experimental multizone model that can be used to validate computational fluid dynamics (CFD) for indoor flow analysis, highlighting the limitations of CONTAM. Tian et al. [13] proposed an algorithm that couples fast fluid dynamics (FFD) and CONTAM to solve problems arising from the well-mixed assumptions of CONTAM. However, these studies focused on improving CONTAM by partially employing CFD, such as solving the air flow in a zone where the momentum effect of air motion is strong. Furthermore, they adopted the Reynolds-averaged Navier-Stokes (RANS) approach for the turbulence model, which did not perform well for highly unsteady flows.

LES has been widely used to investigate the flow characteristics in various situations [14-17]. Zhang et al. [18] confirmed the validity of LES for indoor flow analysis and discussed the characteristics of indoor airflow based on flow fields. Kahn et al. [19] used the lattice Boltzmann method to simulate indoor flows in a hospital room. Auvinen et al. [20] studied the airborne transmission of respiratory pathogens using LES in a restaurant room. However, these studies were confined to the analysis of the indoor airflow in a single room. In this study, we validated the use of LES for indoor flow analysis in a multizone environment and discussed the flow characteristics.

The remainder of this paper is organized as follows. In Sec. 2, we present a numerical method for the analysis of indoor airflow and describe the multizone model used to validate the LES for indoor flow analysis. In Sec. 3, we provide the validation results that compare our simulation results with the chamber facility experimental results and other simulation results, a discussion of flow fields that resolve flow characteristics in a multizone environment, and the relationship between the orifice formula and flux at openings that connect zones. Finally, we present our conclusions in Sec. 4.

2. Statement of the problem

2.1 Numerical method

The present CFD algorithm for indoor flow analysis is based on LES, the immersed boundary method (IBM), and the wall model. The governing equations are the filtered Navier-Stokes equation and energy equations, as follows:

$$\frac{\partial u_i}{\partial t}+\frac{\partial u_i u_j}{\partial x_j}=-\frac{1}{\rho}\frac{\partial p}{\partial x_i}+\frac{\partial}{\partial x_j}\left(-\tau_{ij}+\nu\frac{\partial u_i}{\partial x_j}\right)+g\beta T\delta_{i2}+f_i \quad (1)$$

$$\frac{\partial T}{\partial t}+\frac{\partial T u_j}{\partial x_j}=\frac{\partial}{\partial x_j}\left(-q_j+\alpha\frac{\partial T}{\partial x_j}\right)+s\,. \quad (2)$$

Here, u_i, T, and p denote the filtered velocity, temperature, and pressure, respectively; similarly, ρ, ν, α, and β represent the density, kinematic viscosity, thermal diffusivity, and thermal expansion coefficient of air, respectively. The Boussinesq approximation is used to determine the buoyancy effect. To model τ_{ij}, the constant coefficient Vreman model is adopted and τ_{ij} is modeled using the eddy viscosity ν_T,

$$\tau_{ij}=-2\nu_T S_{ij} \quad (3)$$

with

$$S_{ij}=\frac{1}{2}\left(\frac{\partial u_i}{\partial x_j}+\frac{\partial u_j}{\partial x_i}\right). \quad (4)$$

For the constant coefficient Vreman model, ν_T is modeled as

$$\nu_T=C_v\sqrt{\frac{B_\beta}{\alpha_{ij}\alpha_{ij}}} \quad (5)$$

with

$$\alpha_{ij}=\frac{\partial u_j}{\partial x_i} \quad (6)$$

$$B_\beta=\beta_{11}\beta_{jj}-\beta_{ij}^2 \quad (7)$$

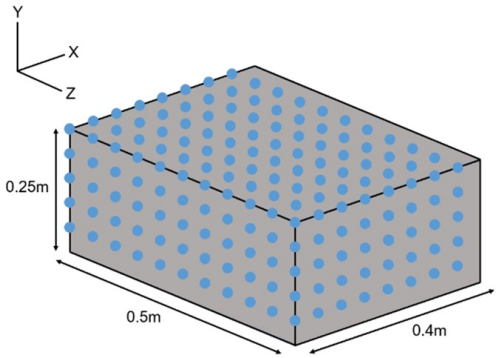

Fig. 1. Distributed Lagrangian points on the block surface in the Eulerian grid of temperature when $\Delta x=\Delta y=\Delta z$ = 0.05 m. Gray surface: block surface, blue circle: Lagrangian point.

$$\beta_{ij}=\sum_{m=1}^{3}\left(\Delta x_m\right)^2\alpha_{mi}\alpha_{mj}\,. \quad (8)$$

Here, Δx_m is the mesh size in the x_m-direction. C_v, the Vreman model coefficient, is set to $2.5C_s^2$, which holds under the assumption that $|S_{ij}|=|\alpha_{ij}|$. The Smagorinsky coefficient C_s is set to 0.2 and its effect on the simulation results is discussed in Sec. 3. To model q_j, the turbulent Prandtl number Pr_T is used as follows:

$$q_j=-\frac{\nu_T}{\mathrm{Pr}_T}\frac{\partial T}{\partial x_j}\,. \quad (9)$$

Pr_T is set to 0.9, which is a widely used value for Pr_T.

To consider solid boundary condition of an object which is called block in this paper, IBM [4, 7, 21] was adopted which elicits f_i and s. For reflecting the geometry of block, Lagrangian points are distributed on the block surface based on the principle that only one Lagrangian point exists in an Eulerian grid cell of fluid variable. In Fig. 1, Lagrangian point distribution on the block surface in the Eulerian grid of temperature when Δx, Δy and Δz equal 0.05 m is shown. For imposing desired boundary condition on block surface, force and heat source are exerted at Lagrangian point $\mathbf{X}_l$. The force and heat source on the Lagrangian point, $F_i(\mathbf{X}_l)$ and $S(\mathbf{X}_l)$ respectively, are given by

$$F_i(\mathbf{X}_l)=\frac{U_i^{des}-U_i(\mathbf{X}_l)}{\Delta t},\ S(\mathbf{X}_l)=\frac{T^{des}-T(\mathbf{X}_l)}{\Delta t} \quad (10)$$

where U_i^{des} = 0 which is no-slip boundary condition and T^{des} is desired temperature on block surface. $U_i(\mathbf{X}_l)$ and $T(\mathbf{X}_l)$ are the interpolated velocity and temperature at the Lagrangian point, respectively. In this study, a linear interpolation is used for calculation of $U_i(\mathbf{X}_l)$ and $T(\mathbf{X}_l)$ as given by

$$U_i(\mathbf{X}_l)=\sum u_i(\mathbf{x})\omega(\mathbf{X}_l-\mathbf{x}),\ T(\mathbf{X}_l)=\sum T(\mathbf{x})\omega(\mathbf{X}_l-\mathbf{x}) \quad (11)$$

with

$$\omega(\mathbf{X}_l - \mathbf{x}) = \left(1 - \frac{|X_l - x|}{\Delta x}\right)\left(1 - \frac{|Y_l - y|}{\Delta y}\right)\left(1 - \frac{|Z_l - z|}{\Delta z}\right) \quad (12)$$

where $u_i(\mathbf{x})$ and $T(\mathbf{x})$ are fluid velocity and temperature at the Eulerian grid point $\mathbf{x}$, respectively. For the distribution of force and heat source on the Lagrangian point to the Eulerian grid point, the same weight is used as follows

$$f_i(\mathbf{x}) = \sum_{l=1}^{N_l} F_i(\mathbf{X}_l)\omega(\mathbf{X}_l - \mathbf{x})\frac{\Delta V(\mathbf{X}_l)}{\Delta v} \quad (13)$$

$$s(\mathbf{x}) = \sum_{l=1}^{N_l} S(\mathbf{X}_l)\omega(\mathbf{X}_l - \mathbf{x})\frac{\Delta V(\mathbf{X}_l)}{\Delta v} \quad (14)$$

where Δv and $\Delta V(\mathbf{X}_l)$ are the volume of an Eulerian grid cell and a Lagrangian point, respectively. N_l is the total number of Lagrangian points.

A wall model based on the log law of the wall-tangential velocity for the insufficient grid resolution near the wall was used as boundary condition of partitions separating zones and surfaces surrounding the computational domain as follows

$$u^+ = \begin{cases} y^+ & for\ y^+ \le 11.635 \\ \frac{1}{\kappa}\ln y^+ + B & for\ y^+ > 11.635 \end{cases} \quad (15)$$

where u^+ is the parallel velocity to the wall normalized by the friction velocity; y^+ is the nondimensional wall-normal distance in wall units; κ = 0.41 and B = 5.5.

The second-order central difference method was used for space discretization. A hybrid three-step Runge-Kutta method was used for time advancement, which treated the convective terms and IBM forcing term explicitly and the subgrid-scale and diffusion terms semi-implicitly. The QUICK scheme was used to calculate the convective terms of the energy equation.

2.2 Simulation model

To validate the results of the LES for indoor flow analysis in a multizone environment and investigate the flow characteristic, we chose two experimental models [12], as shown in Fig. 2. In the first model (Fig. 2(a)), the airflow from zone 1 to the other connected zones is driven by the pressure difference and momentum of the supply airflow. In the second model (Fig. 2(b)), unbalanced airflows arise from the buoyancy effect generated by a block with heat in zone 2. For both models, the computational domain was 6.25 m × 2.45 m × 4.95 m along the x, y and z directions, respectively. The corresponding meshes were set to 125 × 49 × 99 in each direction because simulation results with twice more meshes in all directions showed very little difference. The meshes were uniform in all three directions ($\Delta x = \Delta y = \Delta z = 0.05\ m$) such that all the zero-thickness partitions (blue panels in Fig. 2) fit meshes. Staggered grid were adopted and normal component of the velocity on each partition was set to zero. The flow rates of the supply air in the first model were 0.034, 0.053, 0.105, 0.14, and 0.215 m^3/s.

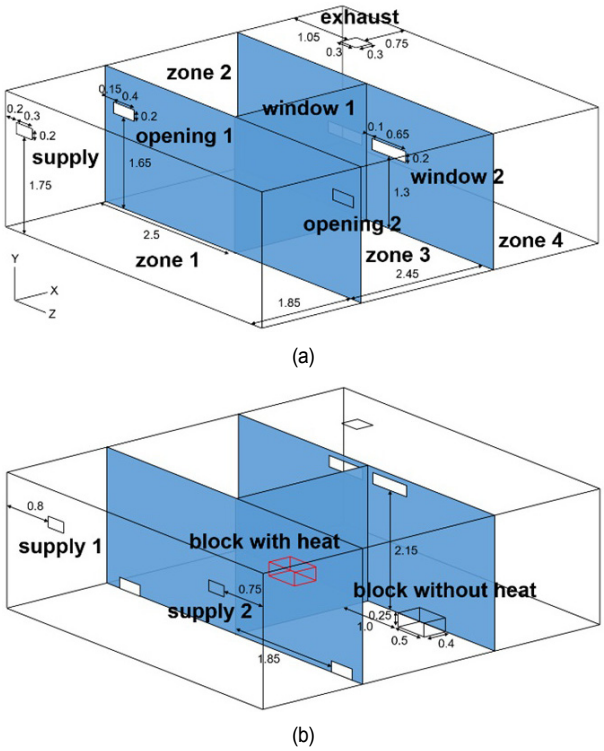

(a)

(b)

Fig. 2. Tested models: (a) distribution of airflow from zone 1 to the other connected zones is influenced by the momentum of the supply airflow; (b) unbalanced distribution of airflow arises from the buoyancy effect generated by the block with a heat source in zone 2. All numbers denote the length in meters.

For the second model, an adiabatic condition was applied for the temperature at most surfaces except for the heated block. Three temperatures of the heated block were considered: 30, 35, and 46 °C. The temperature of the supply air was 18.5 °C. The flow rates of supplies 1 and 2 were both 0.051 m^3/s. For all computations, the time step (Δt) was adjusted to satisfy the Courant-Friedrichs-Lewy (CFL) condition defined by

$$\Delta t \max\left(|u|/\Delta x, |v|/\Delta y, |w|/\Delta z\right) \le 1. \quad (16)$$

Our simulation results were obtained for 40000 time steps after a transient run of 120000 time steps.

3. Results

3.1 Validation of the results

Wang et al. [12] provided the measurement data for limited variables from their chamber facility experiments for the two models and simulations using ANSYS Fluent which is based on $k-\varepsilon$ model for the first model and CFD0 which is their

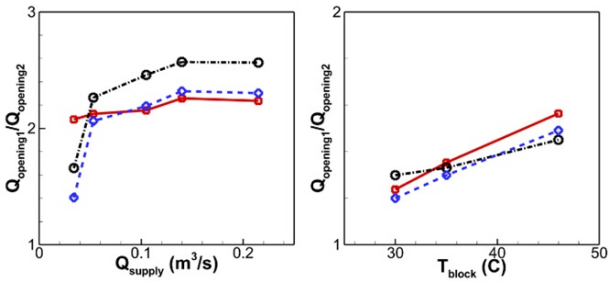

Fig. 3. Ratio of the airflow rates at opening 1 and 2 according to the (a) supply airflow rate in the first model; (b) temperature of the block in the second model. Red line: present result, black dash-dot line: results of chamber facility experiment, blue dashed line: (a) ANSYS result; (b) CFD0 result.

own CFD model for the second model. The ratios of the airflow rates at openings 1 and 2 were measured for various supply airflow rates in the first model and different temperatures of a block with heat in the second model, respectively. Furthermore, measurement data for the mean velocity in the first model and mean temperature in the second model at the chosen locations were available.

In Fig. 3(a), the ratios of the airflow rates at openings 1 and 2 for five different supply airflow rates in the first model from our simulation are compared against the measurements and simulation results using ANSYS [12]. Overall, good agreement with the reference data is obtained, except for the case with a supply airflow rate of 0.034 m^3/s. If we set C_s to 0.08, our simulation yielded a value about 1.6 for all supply flow rates, which is significantly closer to the measured data for supply airflow rate of 0.034 m^3/s only. This sensitivity of simulation result to the value of C_s comes from highly unsteady fluid motion generated by the interaction of supply airflow and opening 1. From these results, we found that the set of appropriate C_s value is important for accurate CFD simulation based on LES when airflow at opening is driven by the momentum of supply airflow. In Fig. 3(b), the ratio of the airflow rate at openings 1 and 2 for different block temperatures in the second model is shown. Good agreement with the reference result is obtained for all cases. For this case, we verified that our simulation results were insensitive to changes of C_s value since airflow at opening in this case is driven by the pressure difference of connected zones, which is fairly stable in this case.

A comparison of the time-averaged profiles of the velocity in the first model and temperature in the second model at the measurement points shown in Fig. 4(a) between our simulation results and the reference results is presented in Fig. 4. Fig. 4(b) shows the mean magnitude of the velocity profile at three measurement points (P1, P2, and P3) located in zone 1. For P1, which is located near the supply inlet, the simulation result shows an underestimated value compared with the reference result at approximately Y/H = 0.6. Our mesh size appears to be slightly large for accurately resolving the fluid motion driven by the momentum of the supply airflow. However, for meas-

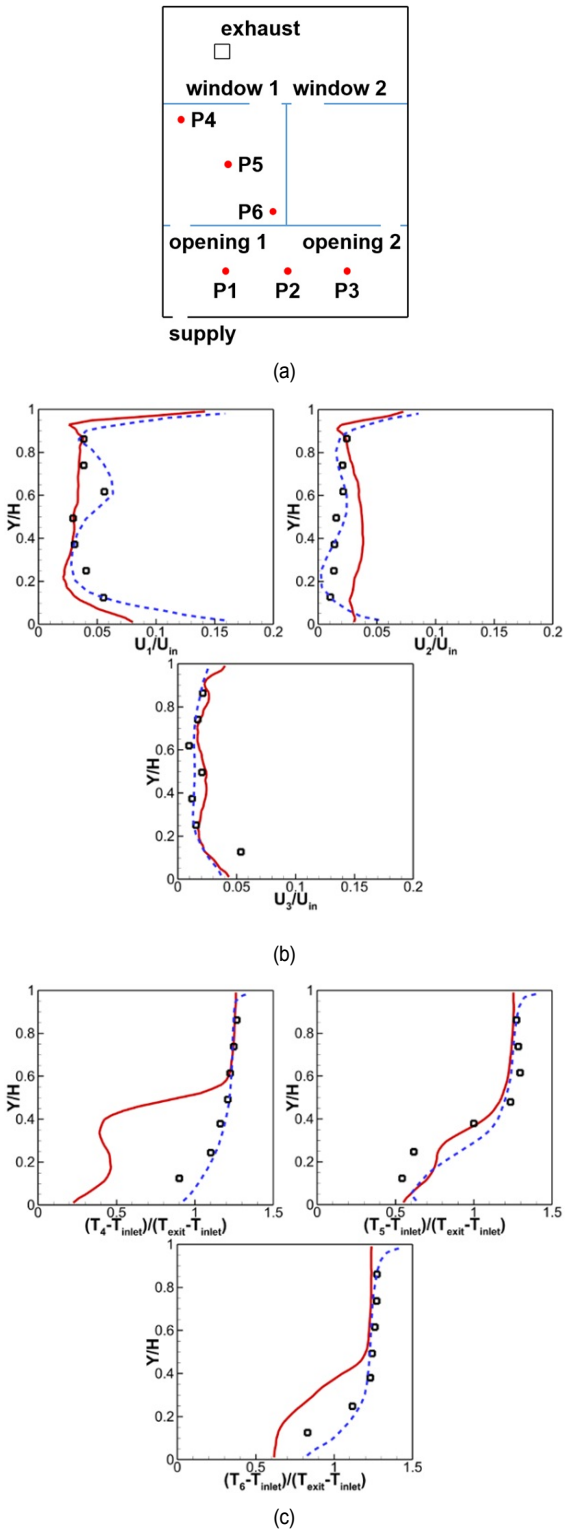

Fig. 4. Results for the time-averaged profile: (a) location of the measurement point; (b) mean magnitude of velocity profile in the first model at P1, 2, and 3; (c) mean temperature profile in the second model at P4, 5, and 6, red line: present result, black symbol: chamber facility experiment result, blue dash in (b) ANSYS result; blue dash in (c) CFD0 result (H = 2.45 m, U_{in} = 2.281 m/s which is the supply air velocity, T_{inlet} = 18.5 °C which is the opening 1 air temperature, T_{exit} = 23 °C which is the window 1 air temperature).

urement point 2, which is located at the center of zone 1, our simulation tends to overestimate the flow around $Y/H = 0.2$. For measurement point 3, the simulation results exhibit very good agreement. Fig. 4(c) shows the mean temperature profiles at three measurement points (P4, P5, and P6) located in zone 2, where the block was heated. For measurement point 4, which faces the airflow at opening 1, our simulation result shows a lower temperature near the bottom owing to the influence of the airflow that carries low-temperature air through opening 1. In Chang et al. [22], they showed that extracted turbulent Prandtl number near the opening is much lower value than 0.9 when the Reynolds number of airflow at opening is low, which means that the convective heat transfer from opening is weak in this case. By this result, we conjectured that the value of Pr_T has strong influence on the simulation result of temperature when confronting the airflow at opening. For measurement points 5 and 6, the temperature is well diffused from the heated block in our CFD simulation, indicating that the IBM is suitable for applying specific boundary conditions. Overall, the asymmetric airflows caused by the buoyancy effect were well captured by the simulation, although thermal diffusion in the lower part of the chamber was relatively underestimated.

3.2 Flow characteristics

In this section, we use the CFD results for the two models discussed in Sec. 3.1 to investigate the flow structure and characteristics of indoor airflow in a multizone environment. For this purpose, we chose cross sections that included the center of the opening or window because these fields adequately represent the flow structure of indoor airflow in the multizone model. For the first model, in which the distribution of airflow from zone 1 to other connected zones is influenced by the momentum of the supply airflow, we present the time-averaged velocity, pressure, and turbulent kinetic energy field for a supply airflow rate of 0.105 m^3/s. For the second model, in which unbalanced distribution of airflow occurs owing to the buoyancy effect generated by the heated block in zone 2, we present the time-averaged velocity, temperature, and pressure field when the temperature of the block is 35 °C.

Fig. 5 shows the two-dimensional (2D) fields of the time-averaged velocity, kinetic energy, and pressure for the first model in the selected cross-sections. As shown in Fig. 5(a), a

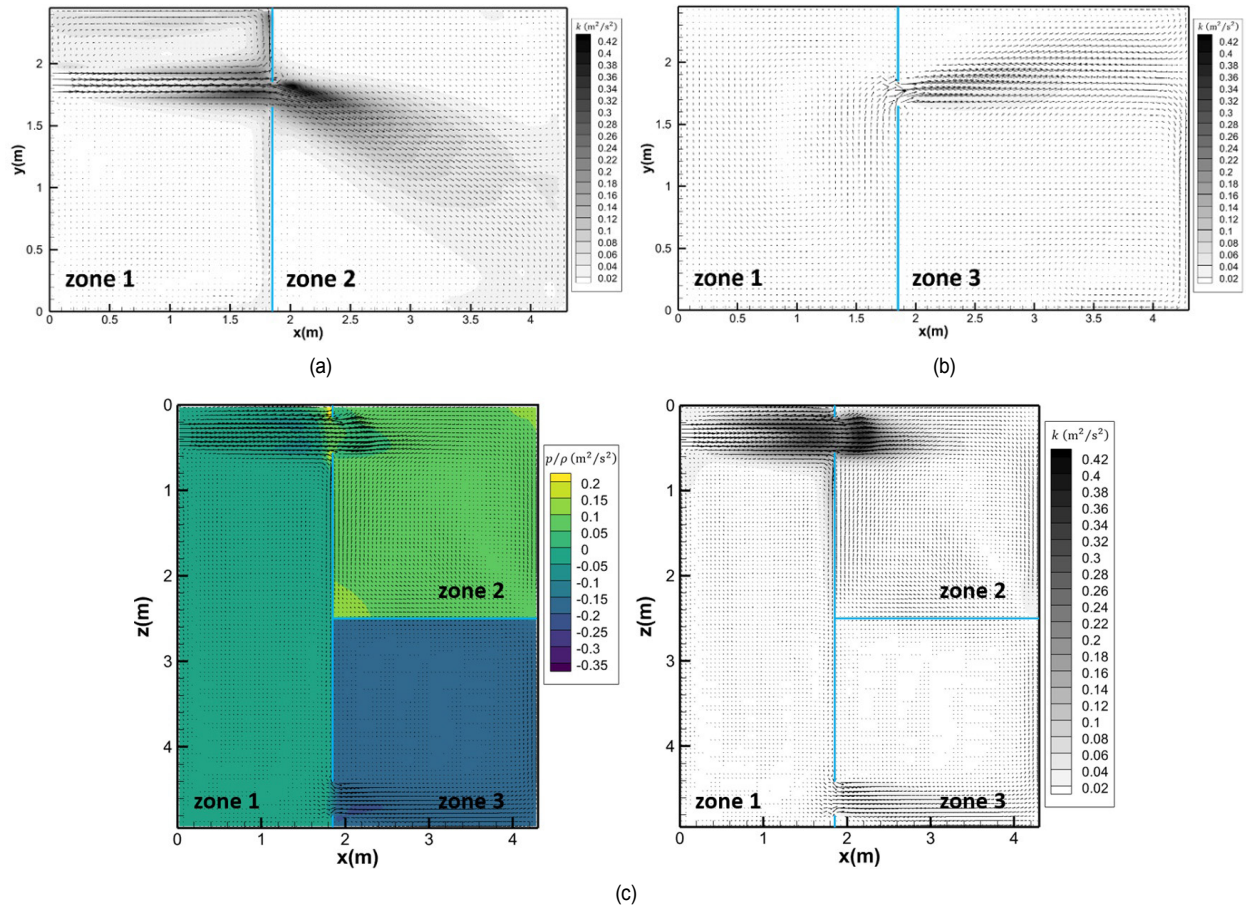

Fig. 5. Two-dimensional mean velocity, pressure, and turbulent kinetic energy field of the first model for zones 1, 2, and 3 at the cross section including the center of (a) the supply and opening 1; (b) the opening 2; (c) the openings 1 and 2, blue line: partition that divides the zones.

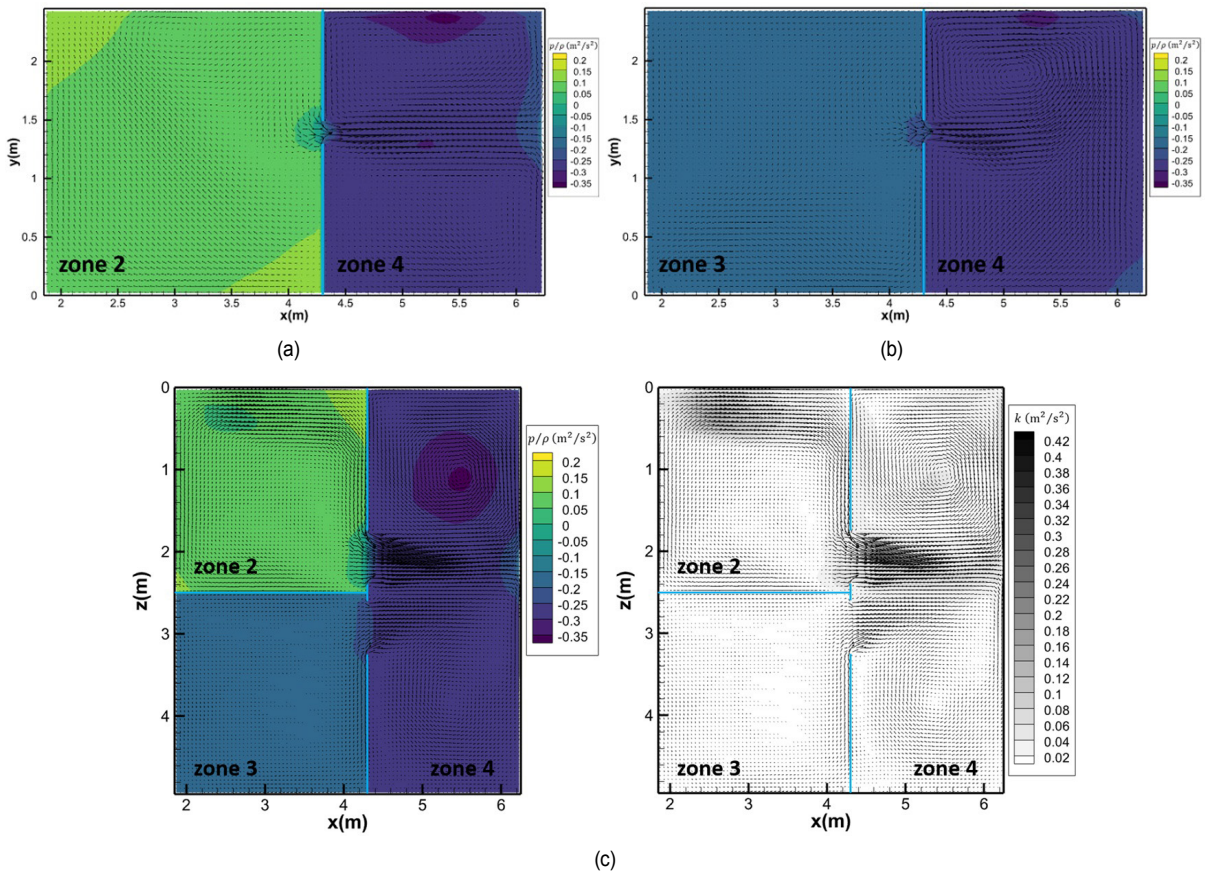

Fig. 6. Two-dimensional mean velocity, pressure, and turbulent kinetic energy fields of the first model for zones 2, 3, and 4 at the cross section including the center of (a) the window 1; (b) the window 2; (c) the windows 1 and 2, blue line: partition that divides the zones.

high turbulent kinetic energy is generated when the supply airflow interacts with opening 1 in zone 1. However, as shown in Fig. 5(b), a relatively low turbulent kinetic energy is generated near opening 2, through which the flow is driven by the pressure difference between the connected zones. The mean velocity distributions in zones 2 and 3 are clearly different: the momentum-driven flow through opening 1 is deflected downward owing to the vertical mismatch in the height of the supply hole and opening 1, whereas the pressure-driven flow remains almost horizontal, with a slight deflection toward the ceiling owing to the Coanda effect. As shown in Fig. 5(c), the pressure distribution on the horizontal plane at the height of the openings clearly indicates that the pressure is almost uniform in each zone and varies significantly across the openings. The mean velocity distribution on the same horizontal plane (Fig. 5(c)) reveals asymmetric jet flows in zones 2 and 3, and the difference between them is more pronounced in the kinetic energy distribution. Another noticeable phenomenon is that except for the strong momentum region in zone 1 and jet flows in zones 2 and 3, the airflows were weak in terms of both the mean velocity and kinetic energy. Fig. 6 shows the 2D fields of the first model for zones 2, 3, and 4. The weak circulatory flow observed in zone 2 is probably caused by the jet flow generated at opening 1, as shown in Fig. 5(a). A relatively weak flow is observed in zone 3, as shown in Fig. 6(b). The two jet flows generated at windows 1 and 2 in zone 4 are comparable because both are induced by the pressure difference across the windows. However, the jet from window 1 is stronger than that from window 2 owing to the difference in the flow rate or equivalent pressure, as shown in the plan view of the flow at the window height in Fig. 6(c). The pressure distribution in each zone is almost uniform, except for the region near the exhaust hole in the ceiling of zone 4. Furthermore, the pressure has a local minimum at the center of another vortex induced by the jet flow at window 1 in zone 4, as shown in Fig. 6(c). These observations confirmed that the pressure in each zone was almost uniform when air flowed through the opening or window owing to the pressure difference, although locally strong jet flows were induced.

The 2D fields of the time-averaged velocity, pressure, and temperature for the second model are shown in Fig. 7. The buoyancy force resulting from the heated block at the bottom of zone 2 induces a vertical pressure gradient, as shown in Fig. 7(a). This pressure gradient then creates a low pressure in the lower part of zone 2 (Fig. 7(b)), which induces a higher flow rate from zone 1 through opening 1 located near the bottom than through opening 2 in zone 3, which breaks the symmetry. The temperature distribution in zone 2 (Fig. 7(a)), clearly indi-

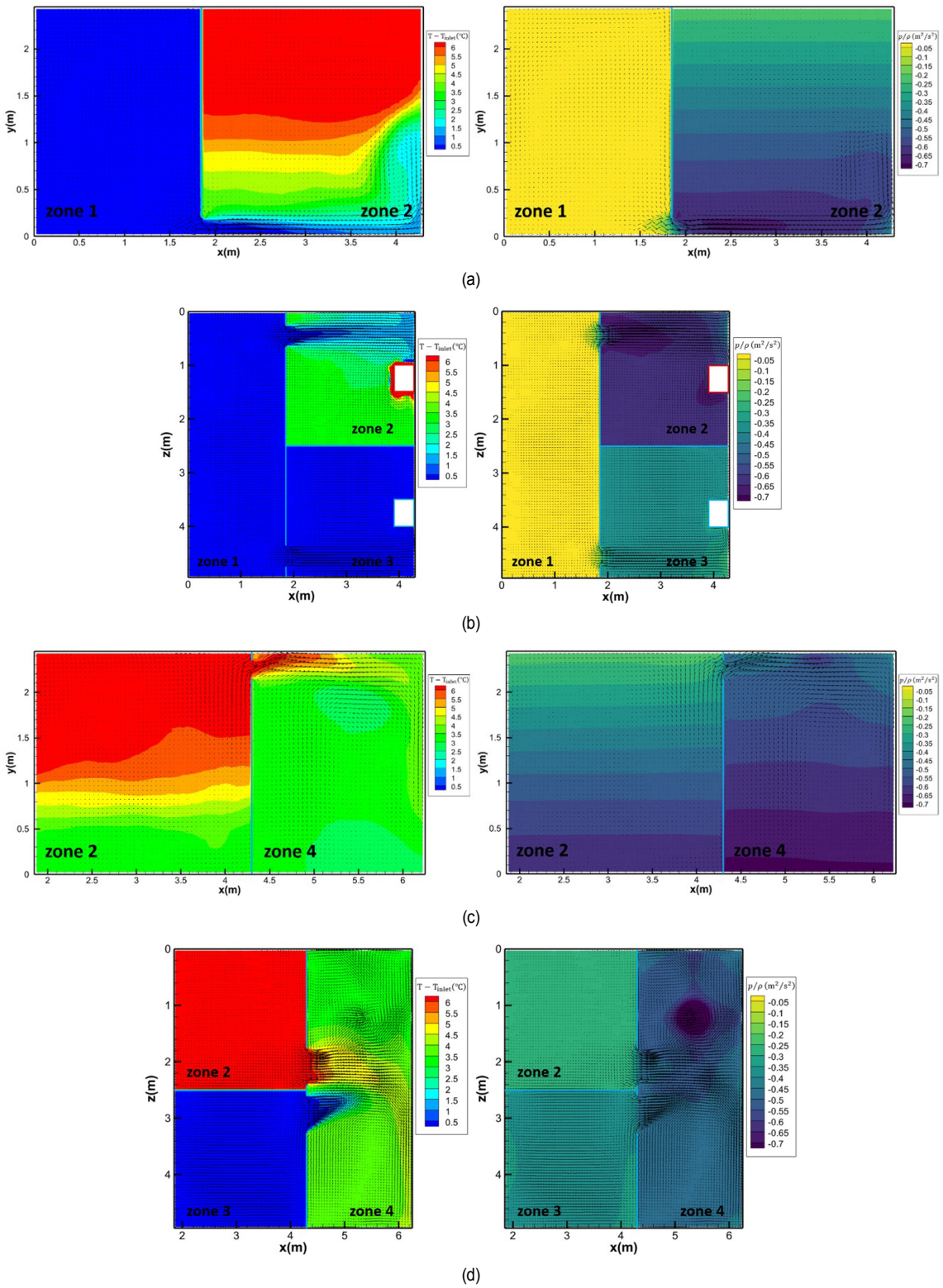

Fig. 7. Two-dimensional mean velocity, temperature, and pressure fields of the second model at the cross section including the center of (a) the opening 1; (b) the openings 1 and 2; (c) the window 1; (d) the windows 1 and 2, blue line: partition that divides the zones, red box : heated block, Blue box : block without heat.

cates the slight distortion of the stratification by the vortex created by the upward flow induced by the heated block. This vortex appears to be responsible for the temperature discrepancy at P4, as shown in Fig. 4(c). As shown in Fig. 7(b), the temperature distribution in the lower parts of zones 2 and 3 confirms that the IBM is suitable for temperature. The tem-

perature in zone 4 becomes strongly stratified near the ceiling and window 1 because of the flow through window 1, resulting in a weak vertical pressure gradient in zone 4 (Fig. 7(c)). The jet from window 1 is deflected toward the ceiling owing to the buoyancy acting on the heated air. The hot jet from window 1 and the cold jet from window 2 in zone 4 mix to create an anticlockwise vortex around the exhaust hole near the ceiling, as shown in Fig. 7(d). This mixing almost homogenized the temperature in zone 4 to the average temperature of the two jets. From the second model, we confirm that for the flow driven by the buoyancy and pressure difference, the pressure is uniform within a zone in the horizontal plane. However, it increases vertically depending on the degree of thermal stratification, and the jet from an opening can be deflected by the buoyancy force.

3.3 Quantification of the flow rate using the orifice model

In a multi-zone environment, the flow rate between two connected zones is the most critical quantity that determines pollutant dispersion. Therefore, accurate quantification of the flow rate is necessary. In network models such as CONTAM, orifice formulae are used to establish the relationship between the flow rate and pressure difference. In this section, we investigate the feasibility of using orifice formula to quantify the flow rate based on the full simulation data. For this purpose, we extracted the coefficient of discharge C_d at each opening through which the flow was driven by the pressure difference between the connected zones. Our investigation of the flow fields in the previous section indicated that the pressure remained uniform within a zone when the flow occurred only because of the pressure difference, and that the pressure increased vertically within a zone when the zone was thermally stratified. Therefore, we chose the geometric center of each zone, more specifically, (0.925 m, 1.225 m, 2.475 m), (3.075 m, 1.225 m, 1.25 m), (3.075 m, 1.225 m, 3.725 m) and (5.275 m, 1.225 m, 2.475 m) in zones 1, 2, 3 and 4, respectively, as the measurement point for the pressure value for calculating the pressure difference between the connected zones for the first model. For the second model, the geometric center was within the horizontal plane at the height of the opening or window, which are (0.925 m, 0.1 m, 2.475 m), (3.075 m, 0.1 m, 1.25 m) and (3.075 m, 0.1 m, 3.725 m) for extracting $C_{d,o1}$ and $C_{d,o2}$, (3.075 m, 2.25 m, 1.25 m), (3.075 m, 2.25 m, 3.725 m) and (5.275 m, 2.25 m, 2.475 m) for extracting $C_{d,w1}$ and $C_{d,w2}$, respectively. At opening 1 of the first model, in which the flow is influenced by the momentum of the supply airflow, we considered this effect in the orifice formula by introducing a velocity scale U_0. This represents the degree of the momentum as follows:

$$Q / A = C_d \sqrt{2\frac{\Delta p}{\rho} + \mathrm{U}_0^2} \tag{17}$$

Table 1. Values of C_d at each opening for the first model.

$\mathrm{Q}_{\mathrm{supply}}\left(\mathrm{m}^3/\mathrm{s}\right)$	$C_{d,o1}$	$C_{d,o2}$	$C_{d,w1}$	$C_{d,w2}$
0.034	0.669	0.684	0.673	0.662
0.053	0.661	0.683	0.677	0.662
0.105	0.661	0.685	0.677	0.661
0.140	0.683	0.683	0.675	0.662
0.215	0.674	0.682	0.677	0.660

Table 2. Values of C_d at each opening for the second model.

$\mathrm{T}_{\mathrm{block}}$ (°C)	$C_{d,o1}$	$C_{d,o2}$	$C_{d,w1}$	$C_{d,w2}$
30	0.650	0.638	0.648	0.656
35	0.650	0.636	0.685	0.688
46	0.650	0.634	0.703	0.679

where Q, A, and Δp are the airflow flux at the opening, area of the opening, and pressure difference between the connected zones, respectively. To measure U_0, we chose the center of opening 1 at x = 1.5 m based on our observations of the flow fields shown in Figs. 5(a) and (b). This is because the jet flow from the supply hole in zone 1 in front of opening 1 is almost uniform up to this point (Fig. 5(a)), and the flow is almost zero when the airflow at opening 2 is driven by the pressure difference only (Fig. 5(b)).

Table 1 lists the values of C_d evaluated at each opening for the first model. The introduction of the momentum effect into the orifice formula for opening 1 yields C_d comparable to those for other openings and windows. The values of C_d are scattered in the relatively narrow range of 0.660–0.685, which is suitable for modeling. Furthermore, C_d is universal with respect to the supply flow rate.

Table 2 lists the values of C_d at each opening for the second model. Overall, the range of C_d is 0.634–0.703, which is slightly wider than that of the first model. The variation in C_d with respect to the block temperature for openings 1 and 2, where the flow occurs owing to the pressure difference, is almost negligibly small. However, C_d fluctuates drastically with the block temperature for windows 1 and 2, through which the flow is affected by the temperature difference. Despite this wide variation, the range of C_d for the second model is not significantly different from that for the first model.

4. Conclusion

In this study, we numerically simulated the indoor airflow for two models in a multizone environment using LES. One model was driven by the pressure difference while the other was driven by the buoyancy caused by heated air. By comparing the simulation results with the available measurement data obtained from a chamber facility [12], we validated the use of LES for indoor flow analysis. We used the simulation results to investigate in detail the flow structure and characteristics of indoor airflow in a multizone environment. In the first model, the

pressure was almost homogenized within each zone, whereas it increased vertically in the heated zone in the second model, in which the air was thermally stratified. Finally, we confirmed that modeling the flow rate through the opening using the orifice formula yielded a relatively universal discharge coefficient for the two models.

In our numerical approach, we simulated the entire domain of an indoor multizone environment by arranging meshes to fit the panels separating zones. The advantage of this approach is that the wall-normal velocity at the panels can be maintained to vanish almost perfectly. However, its disadvantage is the heavy cost of simulations, such as the long simulation time owing to the large size of the matrix. This problem may be addressed by solving the flow in each zone separately, so that the size of the matrix can be reduced. This seems reasonable because the flows in each zone are almost decoupled from each other and connected to each other through a small opening. The flow rate through this opening can then be related to the pressure difference because the discharge coefficient exhibits relatively universal behavior, as discussed in Sec. 3.3. Our findings provide a direction for future studies.

Acknowledgments

This study was supported by the Agency for Defense Development of the Korean Government (Grant No. 912873001).

Nomenclature

u_i : Fluid velocity in the i direction
T : Temperature
p : Pressure
τ_{ij} : Subgrid-scale stress tensor
q_i : Subgrid-scale heat flux
ρ : Density of air
ν : Kinematic viscosity of air
α : Thermal diffusivity of air
β : Thermal expansion coefficient of air
ν_T : Eddy viscosity
C_v : Vreman model coefficient
C_s : Smagorinsky model coefficient
Pr_T : Turbulent Prandtl number
$\mathbf{X}_l$: Position of the Lagrangian point
$\mathbf{x}$: Position of the Eulerian grid point
F_i : Force on the Lagrangian point
S : Heat source on the Lagrangian point
U_i : Interpolated velocity at the Lagrangian point
f_i : Force acting on the fluid because of the IBM
s : Heat source on the fluid because of the IBM
ΔV : Volume represented by a Lagrangian point
Δv : Volume of an Eulerian cell
Q_{supply} : Flow rate of the supply air
T_{block} : Temperature of the heated block
U_0 : Fluid velocity representing the degree of momentum
C_d : Coefficient of discharge

References

[1] P. Gousseau, B. Blocken, T. Stathopoulos and G. J. F. van Heijst, CFD simulation of near-field pollutant dispersion on a high-resolution grid: A case study by LES and RANS for a building group in downtown Montreal, *Atmospheric Environment*, 45 (2) (2011) 428-438.

[2] K. A. Lundquist, F. K. Chow and J. K. Lundquist, An immersed boundary method enabling large-eddy simulations of flow over complex terrain in the WRF model, *Monthly Weather Review*, 140 (2012) 3936-3955.

[3] K. Moon, J. M. Hwang, B. G. Kim, C. Lee and J. Choi, Large-eddy simulation of turbulent flow and dispersion over a complex urban street canyon, *Environmental Fluid Mechanics*, 14 (6) (2014) 1381-1403.

[4] J. Nam and C. Lee, Real-time prediction of urban flow and dispersion, *Journal of Mechanical Science and Technology*, 35 (10) (2021) 4565-4574.

[5] G. Byun and R. L. Simpson, Structure of three-dimensional separated flow on an axisymmetric bump, *AIAA Journal*, 44 (5) (2006) 999-1008.

[6] J. Bao, F. Katopodes and K. A. Lundquist, Large-eddy simulation over complex terrain using an improved immersed boundary method in the weather research and forecasting model, *Monthly Weather Review*, 146 (9) (2018) 2781-2797.

[7] J. Nam and C. Lee, An immersed boundary method for complex terrain flow analysis, *Journal of Mechanical Science and Technology*, 36 (4) (2022) 1817-1824.

[8] L. L. Wang, W. S. Dols and Q. Chen, Using CFD capabilities of CONTAM 3.0 for simulating airflow and contaminant transport in and around buildings, *HVAC&R Research*, 16 (6) (2010) 749-763.

[9] L. C. Ng, A. Musser, A. K. Persily and S. J. Emmerich, Multizone airflow models for calculating infiltration rates in commercial reference buildings, *Energy and Buildings*, 58 (2013) 11-18.

[10] W. S. Dols and B. J. Polidoro, *CONTAM User Guide and Program Documentation Version 3.2*, *NIST Technical Note 1887*, NIST, USA (2015).

[11] K. Verijkazemi, N. Mansouri, F. Moattar and S. M. Khezri, Evaluation of indoor PM distribution by CONTAM airflow model and real time measuring: model description and validation, *Avicenna Journal of Environmental Health Engineering*, 5 (1) (2018) 42-49.

[12] L. Wang and Q. Chen, Validation of a coupled multizone-CFD program for building airflow and contaminant transport simulations, *HVAC&R Research*, 13 (2) (2007) 267-281.

[13] W. Tian, T. A. Sevilla, W. Zuo and M. D. Sohn, Coupling fast fluid dynamics and multizone airflow models in Modelica buildings library to simulate the dynamics of HVAC systems, *Building and Environment*, 122 (2017) 269-286.

[14] B.-G. Kim, C. Lee, S. Joo, K.-C. Ryu, S. Kim, D. You and W.-S. Shim, Estimation of roughness parameters within sparse urban-like obstacle arrays, *Boundary-Layer Meteorology*, 139 (2011) 457-485.

[15] S. T. Bose and G. I. Park, Wall-modeled large-eddy simulation for complex turbulent flows, *Annual Review of Fluid Mechanics*, 50 (2018) 535-561.
[16] S. Won and C. Lee, Simulation of the mushroom cloud generated from a high-energy explosion using large-eddy simulation, *Journal of Mechanical Science and Technology*, 34 (6) (2020) 2443-2453.
[17] A. Cellier, F. Duchaine, T. Poinsot, G. Okyay, M. Leyko and M. Pallud, An analytically reduced chemistry scheme for large eddy simulation of lithium-ion battery fires, *Combustion and Flame*, 250 (2023) 112648.
[18] W. Zhang and Q. Chen, Large eddy simulation of indoor airflow with a filtered dynamic subgrid scale model, *International Journal of Heat and Mass Transfer*, 43 (17) (2000) 3219-3231.
[19] M. A. I. Khan, N. Delbosc, C. J. Noakes and J. Summers, Real-time flow simulation of indoor environments using lattice Boltzmann method, *Building Simulation*, 8 (2015) 405-414.
[20] M. Auvinen, J. Kuula, T. Gronholm, M. Suhring and A. Hellsten, High-resolution large-eddy simulation of indoor turbulence and its effect on airborne transmission of respiratory pathogens-model validation and infection probability analysis, *Physics of Fluids*, 34 (1) (2022) 015124.
[21] J. Jang and C. Lee, An immersed boundary method for non-uniform grids, *Journal of Computational Physics*, 341 (2017) 1-12.
[22] K. A. Chang and E. A. Cowen, Turbulent Prandtl number in neutrally buoyant turbulent round jet, *Journal of Engineering Mechanics*, 128 (10) (2002) 1082-1087.

Jaewook Nam received his B.S. (2018) in Mechanical Engineering from Yonsei University, Seoul, Korea. He is an integrated Ph.D. student at the School of Mathematics and Computing, Yonsei University, Korea. His research interests include large-eddy simulation, immersed boundary methods, and the area of incompressible fluid dynamics.

Hyunwoo Nam received his Ph.D. in 2016 from the Electrical Engineering department at Columbia University. His professional interests are in the analysis of video streaming and intelligent content delivery over wireless networks. During his Ph.D., his collaboration with Bell Labs and Verizon focused on capacity planning for wireless networks, and future networks such as SDN and NFV for intelligent content delivery over wireless. His research works include CBR dispersion modeling and early warning detection system at Agency for Defense Development (ADD) in South Korea.

Changhoon Lee received his B.S. (1985) and M.S. (1987) degrees from Seoul National University, Seoul, Korea and Ph.D. (1993) in Mechanical Engineering from UC Berkeley, USA. He is a Professor at the School of Mathematics and Computing and Department of Mechanical Engineering, Yonsei University, Korea. His research interests include fundamentals of turbulence, particle-turbulence interaction, deep learning of turbulence, numerical algorithms, air pollution modeling, and stochastic process.